Synthesis, Optical Properties, and Electrochemical Behavior of 5,10,15,20-Tetraaryl-5,15-diazaporphyrin-Amine Hybrids

Yuna Satoh,[b] Yutaro Fujita,[a] Naoya Muramatsu,[b] Ko Furukawa,[c] Tadaaki Ikoma,[a] Mao Minoura,[d] Haruyuki Nakano,[e] and Yoshihiro Matano*[a]

This work reports a series of covalently linked hybrids comprising 5,10,15,20-tetraaryl-5,15-diazaporphyrinoids (M-TADAP; M = Ni, Zn, Cu) and amines. M-TADAP-amine hybrids were prepared via the metal-templated cyclization of the corresponding metal(II)-dipyrrin complexes and redox reactions on the DAP unit. In the UV/vis/near-IR absorption spectra of the hybrids containing an 18π-electron DAP ring, broad charge-transfer bands were observed, reflecting the electron-donating property of the *para*-aminophenyl groups and the electron-accepting property of the 18π TADAP dication. The electrochemical behavior of the M-TADAP-amine hybrids was strongly dependent on the structure of the peripheral amine units. Further electrochemical oxidation of the hybrids bearing *N*-Ph groups conceivably generated amine-centered radicals, which sequentially underwent irreversible coupling to form benzidine-linked M-TADAP polymer films. The Ni-TADAP-benzidine polymer exhibited the electric conductivity of 1×10^{-3} S m^{-1}.

Introduction

Covalently linked porphyrin-amine hybrids have become increasingly prevalent in the field of materials chemistry owing to their excellent optical properties associated with the readily tunable redox properties of each component. To date, various types of porphyrins carrying multiple peripheral amine auxiliaries have been designed and synthesized.[1] On the one hand, porphyrin-amine hybrids serve as ultraviolet-visible-near infrared (UV/vis/NIR) light-harvesting photosensitizers and electron donors in optoelectronic applications, such as dye-sensitized solar cells.[1e–g,i] On the other hand, the peripheral amine units in the hybrids provide reaction sites for chemical functionalization. For example, electrochemical oxidation at the tertiary amine center of 5,10,15,20-tetrakis(4-*N*,*N*-diphenylaminophenyl) porphyrins **P1** induces polymerization via C–C coupling of the generated ammoniumyl radicals as a key step, producing benzidine-linked porphyrin polymers (porphyrin-benzidine polymers).[2–12] The resulting polymer films exhibit porphyrin- and benzidine-derived optical and redox properties, such as electrochromism, electrical conduction, and electrochemical photocurrent conversion. In some cases, however, the electrochemical oxidation processes of the porphyrin ring (18π Por/17π Por$^{\bullet+}$) and tertiary amine unit ($R_3N/R_3N^{\bullet+}$) in **P1** overlapped each other within narrow voltage ranges, complicating the discrimination of their redox-coupled properties. The separation of porphyrin-centered redox processes from amine-centered processes is therefore of great significance for expanding the applicability of these types of hybrids and enabling the construction of optoelectronic materials capable of responding to wide voltage ranges.

As a scaffold that is structurally similar to **P1** with an intrinsically electron-deficient character, 5,15-diazaporphyrin (DAP)[13] could offer a promising platform for the construction of new porphyrin-amine hybrids with distinctive redox behavior. Recently, we have reported several examples of 5,10,15,20-tetraaryl-5,15-diazaporphyrinoids (TADAPs) **P2** (Scheme 1) and their derivatives.[14–17] The most remarkable feature of TADAPs is their extraordinary air-stability in the 19π-electron ($z=1$) state, which is reversely switchable with the 20π-electron ($z=0$) and 18π-electron ($z=2$) states. In the 18π dication of **P2**, both the highest occupied molecular orbital (HOMO) and lowest unoccupied molecular orbital (LUMO) are stabilized by approximately 2 eV compared with the corresponding orbitals of isoelectronic 5,10,15,20-tetraarylporphyrins, because the unshared electron pairs of the *meso*-nitrogen atoms in **P2** alter the net charge of two electrons. In this regard, TADAPs appear to be promising candidates for the development of unprecedented porphyrin-based redox-mediators, photosensitizers, and conductive materials. During our comprehensive studies on TADAPs, we found

[a] Y. Fujita, Prof. Dr. T. Ikoma, Prof. Dr. Y. Matano
Department of Chemistry, Faculty of Science,
Niigata University
Nishi-ku, Niigata 950-2181 (Japan)
E-mail: matano@chem.sc.niigata-u.ac.jp
[b] Y. Satoh, N. Muramatsu
Department of Fundamental Sciences
Graduate School of Science and Technology,
Niigata University
Nishi-ku, Niigata 950-2181 (Japan)
[c] Prof. Dr. K. Furukawa
Center for Coordination of Research Facilities
Institute for Research Promotion
Niigata University
Nishi-ku, Niigata 950-2181 (Japan)
[d] Prof. Dr. M. Minoura
Department of Chemistry
College of Science,
Rikkyo University
Toshima-ku, Tokyo 171-8501 (Japan)
[e] Prof. Dr. H. Nakano
Department of Chemistry
Graduate School of Science,
Kyushu University
Nishi-ku, Fukuoka 819-0395 (Japan)

Supporting information for this article is available on the WWW under https://doi.org/10.1002/cplu.202100429

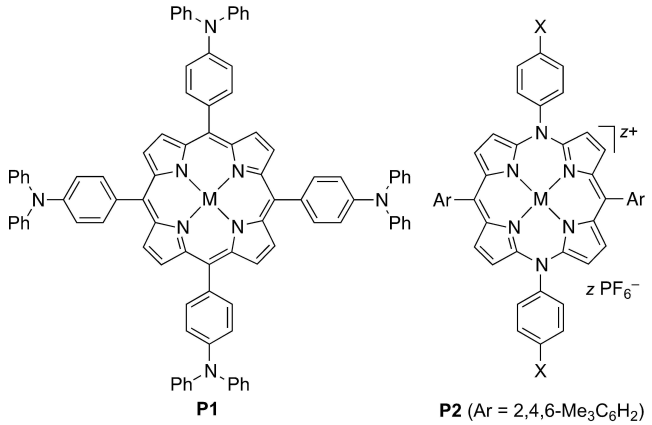

Scheme 1. Porphyrin-amine hybrid (**P1**) and M-TADAP (**P2**; $z = 0$, 1, 2). M=Ni, Cu, etc.

that the introduction of an amino substituent at the *para* position of the *meso*-*N*-phenyl groups (X = NMe_2 or NPh_2) exerted a significant effect on their optical and electrochemical properties.[17] It was confirmed that these electron-donating amino substituents behave as peripheral redox centers, as observed for related porphyrin-amine hybrids.[4] Notably, the redox couples of the TADAP π-electron system were well-separated from those of the amine units owing to the low-lying HOMO of the 18π TADAP dication. This contrasts markedly with the redox behavior of their porphyrin counterparts, which usually give rise to overlapped voltammograms of the porphyrin and amine units, as mentioned above. In addition, we observed that the Ni-TADAP-triphenylamine (TPA) hybrid (**P2**; M = Ni, X = NPh_2) polymerized during electrochemical oxidation to form a polymer film on the electrode. With these preliminary results in hand, we envisaged that both TADAP-amine hybrid monomers and polymers could be applied for the construction of azaporphyrin-based redox-active materials that undergo well-separated redox processes and operate over a wide range of voltages.

Herein we report the synthesis, optical properties, redox behavior, and electropolymerization of a series of M-TADAP-amine hybrids (M = Ni, Zn, Cu) bearing two or four tertiary/secondary amine units at the *meso* positions. The electronic and structural effects of the central metals and peripheral amine units on the optical and electrochemical properties of these hybrids are discussed on the basis of both experimental and theoretical results. Furthermore, the potential utility of the M-TADAP-benzidine polymers as electrical conductors is demonstrated for the first time.

Results and Discussion

Synthesis

New M-TADAP-amine hybrids **3M**–**5M** (M=Ni, Zn, Cu) were prepared according to general procedures reported for the synthesis of related M-TADAPs including **3Ni-a**, **4Ni-a**, and **5Ni-a**.[14,17] Treatment of 1-arylamino-9-chloro-5-mesityldipyrrins **1b**,**c** (mesityl = 2,4,6-trimethylphenyl) with 0.5 equiv. of nickel(II) acetate afforded the corresponding nickel(II)-bis(dipyrrin) complexes **2Ni-b**,**c** (Scheme 2). Metal-templated annulation of **2Ni-b**,**c** using K_2CO_3 in DMF afforded the 20π Ni-TADAP-amine hybrids **3Ni-b**,**c**. One- and two-electron oxidation reactions of **3Ni-b**,**c** with $AgPF_6$ yielded 19π radical cations **4Ni-b**,**c** and 18π dications **5Ni-b**,**c**, respectively. Similarly, zinc(II)-bis(dipyrrin) complexes **2Zn-a**,**b**, obtained from **1a**,**b** and zinc(II) acetate, were converted to 20π Zn-TADAP-amine hybrids **3Zn-a**,**b** using NaO*t*Bu and toluene as the base and solvent, respectively. In contrast to **3Ni-a**,**b**, **3Zn-a**,**b** were gradually oxidized in air. Therefore, Zn-TADAP-amine hybrids were isolated as the 19π radical cations **4Zn-a**,**b** after treatment of **3Zn-a**,**b** with 1 equiv. of $AgPF_6$. Further oxidation of **4Zn-a**,**b** with $AgPF_6$ afforded the 18π dications **5Zn-a**,**b**.

The 19π Cu-TADAP-amine hybrids **4Cu-a**–**c** were directly obtained via the reaction of **1a**–**c** with 1 equiv. of copper(II) acetate in CH_2Cl_2-MeOH followed by anion-exchange with KPF_6 (Scheme 3). Oxidation of **4Cu-a**–**c** with 1 equiv. of $AgPF_6$ afforded the corresponding 18π dications **5Cu-a**–**c**. Notably, all of the 19π radical cations **4M** were isolated as extremely air-

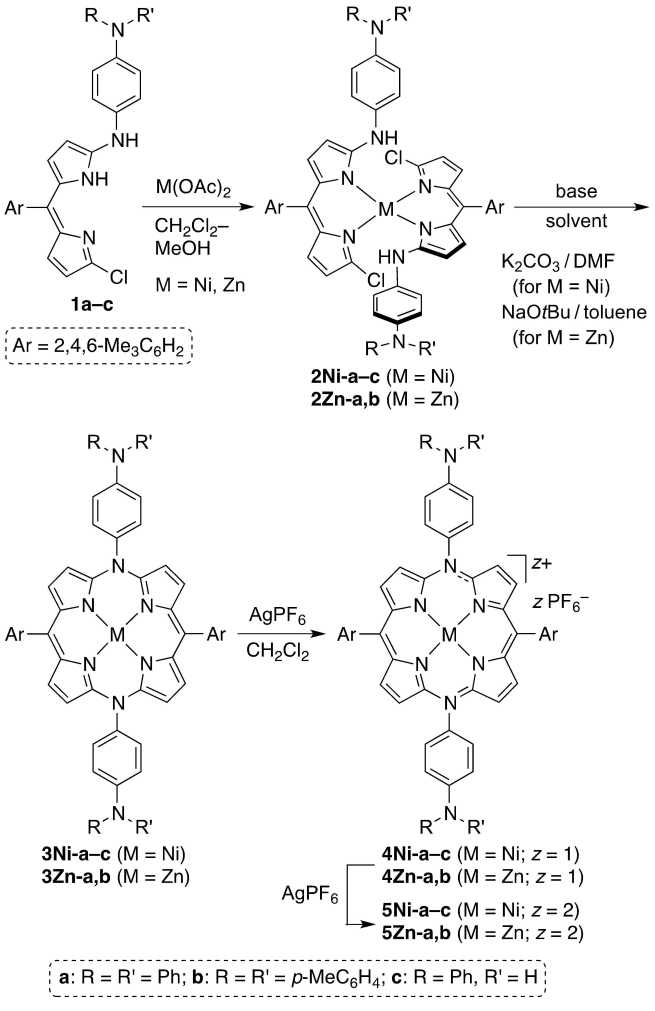

Scheme 2. Synthesis of M-TADAP-amine hybrids **3M**, **4M**, and **5M** (M=Ni, Zn).

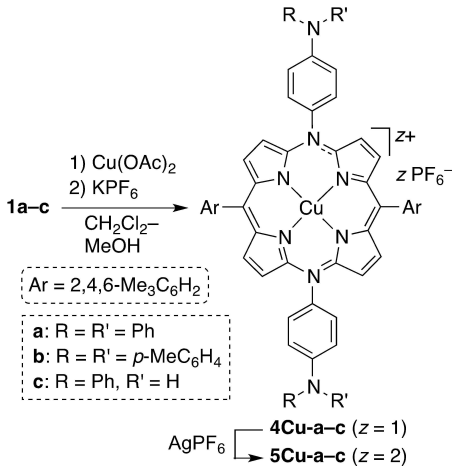

Scheme 3. Synthesis of Cu-TADAP-amine hybrids **4Cu** and **5Cu**.

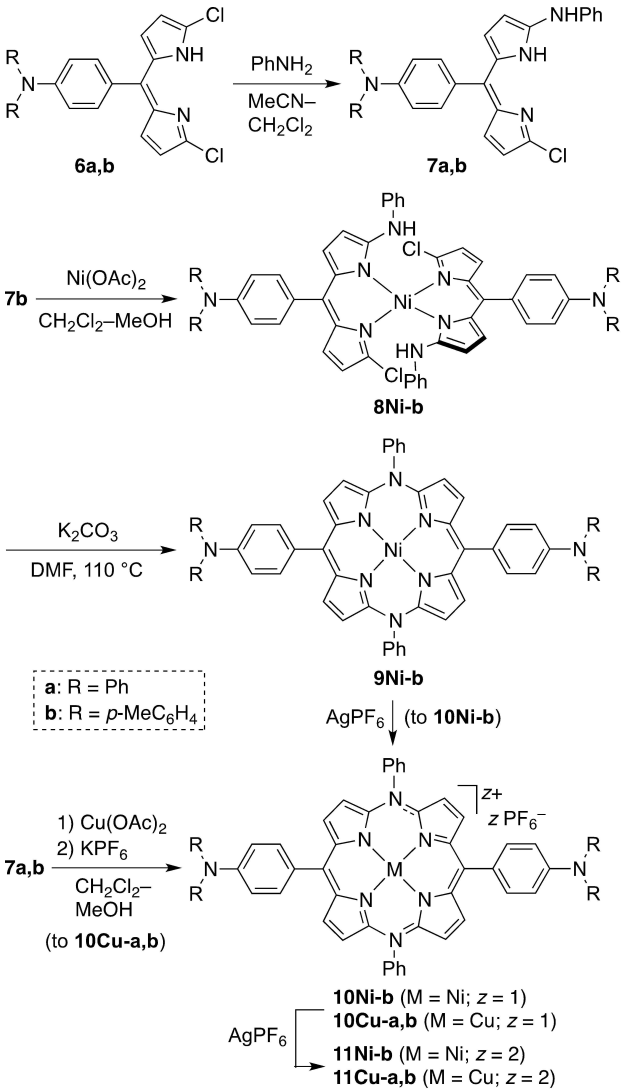

Scheme 4. Synthesis of M-TADAP-amine hybrids **9Ni-b**, **10M**, and **11M** (M=Ni, Cu).

stable dark brown solids and are storable in the solid state over several months under ambient conditions, owing to the positive charge of the DAP ring and efficient delocalization of an unshared electron spin therein (vide infra).

To reveal the effect of substitution sites for the amine units on the optical and redox properties of M-TADAP-amine hybrids, regioisomers bearing the tertiary amine units on the *meso*-C atoms, **9Ni**, **10M**, and **11M** (M = Ni, Cu), were also synthesized (Scheme 4). 5-Aryl-1,9-dichlorodipyrrins **6a**,**b** reacted with aniline in MeCN-CH_2Cl_2 to afford 5-aryl-1-chloro-9-phenylaminodipyrrins **7a**,**b**. Treatment of **7b** with nickel(II) acetate gave the nickel(II)-bis(dipyrrin) complex **8Ni-b**, which was then transformed to the 20π Ni-TADAP-amine hybrid **9Ni-b** via base-promoted Ni-templated cyclization. Oxidation of **9Ni-b** with an appropriate amount of $AgPF_6$ afforded the 19π radical cation **10Ni-b** and the 18π dication **11Ni-b**. The sequential reactions of **7a**,**b** with copper(II) acetate and KPF_6 yielded the corresponding 19π Cu-TADAP-amine hybrids **10Cu-a**,**b**, which were further converted to the 18π dications **11Cu-a**,**b** via oxidation with $AgPF_6$. In addition, Cu-TADAP-amine hybrids containing four *meso*-TPA units, **13Cu** and **14Cu**, were prepared (Scheme 5). The reaction of **6a** with *N*,*N*-diphenylbenzene-1,4-diamine in MeCN-CH_2Cl_2 gave 1,5-diaryl-9-chlorodipyrrin **12**, which underwent Cu-templated cyclization-oxidation reactions to afford **13Cu** and **14Cu**. The 19π radical cations **10M** and **13Cu** were also isolated as air-stable dark brown solids.

Characterization

Newly prepared M-TADAP-amine hybrids **3M**, **4M**, **5M**, **9Ni**, **10M**, **11M**, **13Cu**, and **14Cu** (M = Ni, Zn, Cu) and their precursors were characterized employing NMR and IR spectroscopy, high-resolution electrospray ionization mass (HR-ESIMS) spectrometry, and X-ray crystallography (for **4Cu-c**). In the HR-ESIMS spectra, the molecular ions (for the 20π M-TADAP derivatives) or fragment ions (for the 19π and 18π M-TADAP derivatives) were detected as intense peaks. In the ^{1}H NMR spectra of the 20π and 18π M-TADAP derivatives, **3Ni**/**9Ni** and **5M** (M = Ni, Zn), paratropic and diatropic ring-current effects were observed, respectively, for their pyrrolic β-proton signals (Figure S1 in the Supporting Information).[18] These spectral features clearly indicate the antiaromatic and aromatic character of the DAP rings in **3Ni**/**9Ni** and **5M**, respectively. The chemical shifts of the pyrrolic β-proton signals of **3Ni-b** (3.55/4.68 ppm) were shifted upfield compared with those of **9Ni-b** (3.51/5.05 ppm), implying that the paratropic ring current effects of the 20π *meso*-*N*-TA derivative **3Ni-b** are slightly stronger than those of the 20π *meso*-*C*-TA derivative **9Ni-b**.

The crystal structure of **4Cu-c** was unambiguously elucidated using X-ray crystallography. As shown in Figure 1, **4Cu-c** possesses a distinctly flat DAP π-plane with a root-mean-square deviation of 0.022 Å (total 24 C/N atoms), wherein the copper center adopts square planar geometry. This indicates that the unpaired electron is delocalized over the DAP ring (vide infra). The *meso*-aryl groups are almost perpendicular to the DAP ring

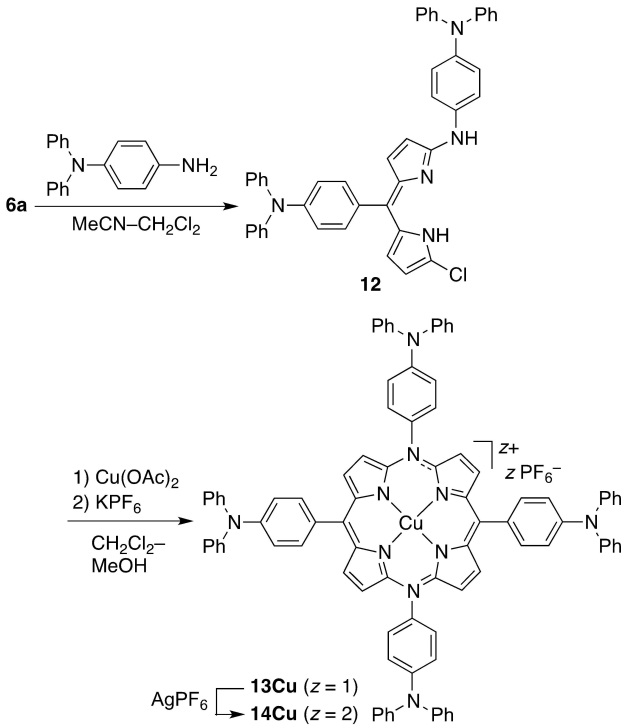

Scheme 5. Synthesis of Cu-TADAP-amine hybrids **13Cu** and **14Cu**.

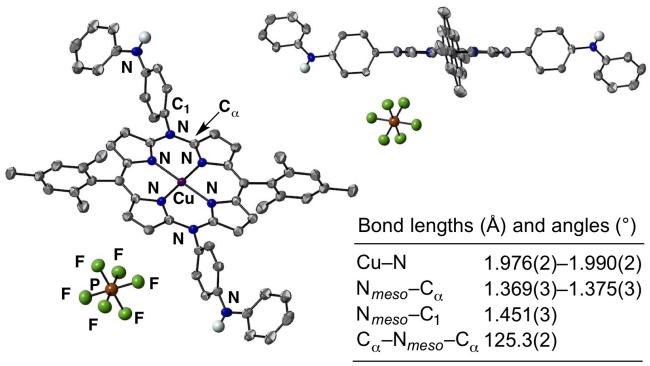

Bond lengths (Å) and angles (°)	
Cu–N	1.976(2)–1.990(2)
N_{meso}–C_α	1.369(3)–1.375(3)
N_{meso}–C_1	1.451(3)
C_α–N_{meso}–C_α	125.3(2)

Figure 1. Top and side views (50% probability ellipsoids) of **4Cu-c**. Hydrogen atoms except for NH groups are omitted for clarity.

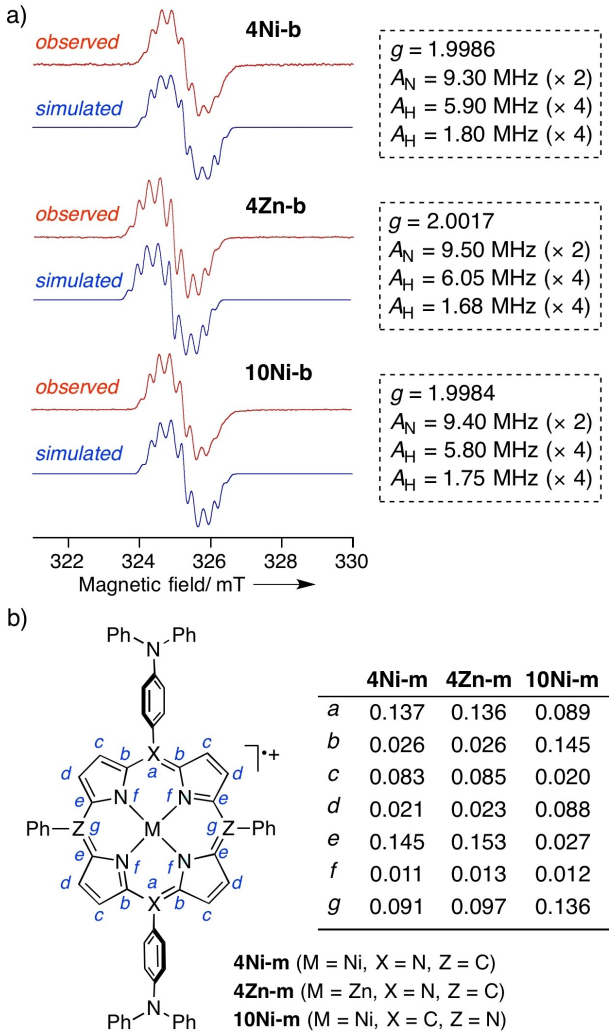

Figure 2. a) EPR spectra of **4Ni-b**, **4Zn-b**, and **10Ni-b** observed in CH_2Cl_2 and hyperfine coupling constants (A_X; X = ^{14}N, ^{1}H) obtained by simulation. b) Average spin densities of 19π radical cations of M-TADAP-TPA **4Ni-m**, **4Zn-m**, and **10Ni-m**.

(dihedral angles = 77.7–88.5°), suggesting that π-conjugation between the *meso*-aryl groups and the DAP ring is negligible. The average *meso*-N–Cα bond length (1.37 Å) is shorter than the *meso*-N–C1 bond length (1.45 Å), which indicates that the unshared electron pairs in the p orbitals of the *meso*-N atoms are effectively conjugated with the π-orbitals of the adjacent pyrrolic α-carbon atoms.

The electron-spin distribution patterns of the 19π radical cations **4Ni-b**, **4Zn-b**, and **10Ni-b** were investigated employing electron paramagnetic resonance (EPR) spectroscopy and density functional theory (DFT) calculations. As shown in Figure 2, these radicals exhibited EPR signals in CH_2Cl_2 at room temperature with *g* values of 1.9986, 2.0017, and 1.9984, respectively. The difference in the *g* values presumably corresponds to the differing electronegativities of nickel and zinc.[19] All of the EPR spectra displayed similar splitting patterns, and the observed hyperfine structures were derived primarily from the two ^{14}N nuclei at the *meso* positions and the eight ^{1}H nuclei on the pyrrolic β-carbon atoms. The calculated spin densities of their model derivatives **4Ni-m**, **4Zn-m**, and **10Ni-m**, in which the *meso*-mesityl and *meso*-tolyl (tolyl = 4-methylphenyl; Tol) groups were replaced by phenyl groups, suggested that the unshared electron spin was not distributed on the peripheral amine moieties but delocalized over the DAP ring. The EPR spectra and DFT calculation results revealed that the electron-spin delocalization patterns of the 19π TADAP radical cations were appreciably influenced by the central metal, but minimally influenced by the position of the *meso*-TPA moieties.

Optical Properties. The UV/vis/NIR absorption spectra of M-TADAP-amine hybrids in CH_2Cl_2 are shown in Figures 3 and S3–S5. Table 1 summarizes the experimentally obtained optical data for the M-TADAP-amine hybrids. These compounds

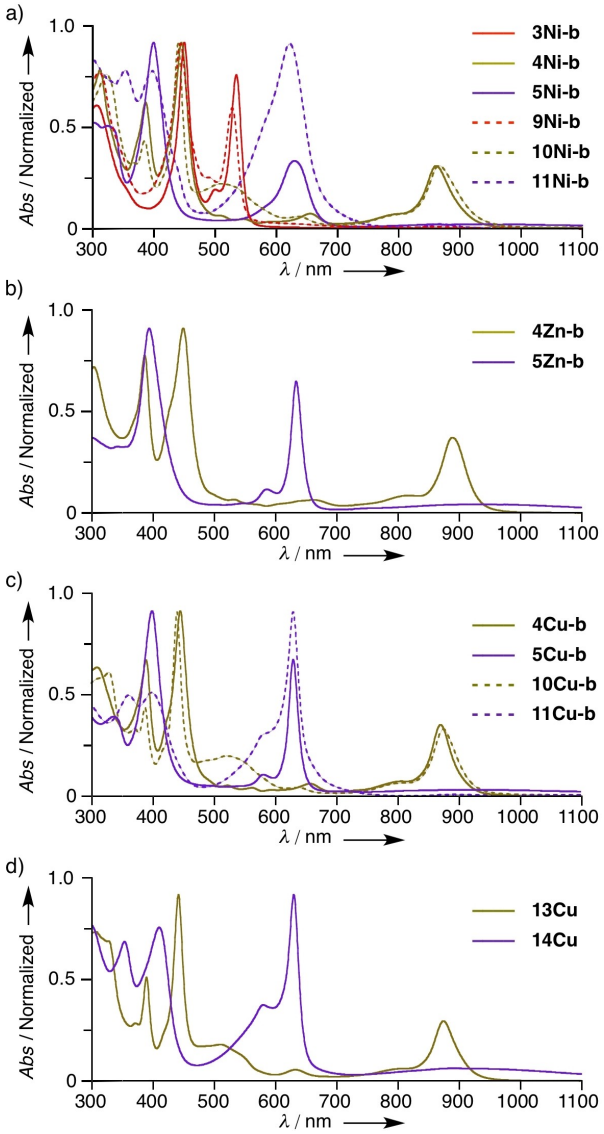

Figure 3. UV/vis/NIR absorption spectra of a) **3**, **4**, **5**, **9**, **10**, **11Ni-b**, b) **4**, **5Zn-b**, c) **4**, **5**, **10**, **11Cu-b**, and d) **13Cu**, **14Cu** in CH_2Cl_2.

Table 1. The absorption maxima (λ_{max}) of M-TADAP-amine hybrids.[a]

Compd	a	b	c
3Ni	448, 533 [b]	449, 534	447, 533
3Zn	447, 522	448, 523	–
4Ni	385, 444, 861 [b]	386, 444, 861	384, 444, 860
4Zn	386, 449, 892	386, 449, 890	–
4Cu	388, 444, 872	388, 445, 871	387, 444, 870
5Ni	400, 626, 863 [b]	399, 629	398, 625
5Zn	394, 634, 820	393, 634, 935	
5Cu	399, 629, 818	397, 631, 939	398, 630, 820
9Ni	–	444, 529	–
10Ni	–	386, 441, 871	–
10Cu	388, 440, 875	389, 441, 878	–
11Ni	–	353, 399, 627	–
11Cu	352, 407, 629, 814	361, 400, 631, 881	–
13Cu	389, 441, 875	–	–
14Cu	353, 410, 630 889	–	–

[a] Measured in CH_2Cl_2. $\lambda_{max} > 350$ nm are listed. *p*-NR_2 = *p*-NPh_2 (**a**), *p*-$NTol_2$ (**b**), *p*-NHPh (**c**). [b] Data from ref. 17.

exhibited plural intense absorption bands in the visible and NIR regions, characteristic of the 20π- (**3M** and **9M**), 19π- (**4M**, **10M**, and **13Cu**), and 18π-electron (**5M**, **11M**, and **14Cu**) states of M-TADAP chromophores. For all three π-electron systems, the central metal exerted a minimal impact on the absorption maxima (λ_{max}).

As previously observed for **5Ni-a**, the absorption spectra of the 18π M-TADAP-amine hybrids **5M**, **11M**, and **14Cu** displayed significantly broad bands in the NIR region, assigned to intramolecular charge-transfer (ICT) transitions from the amine-based HOMO to the DAP-based LUMO, according to the results of time-dependent-DFT (TD-DFT) calculations (Figures 4 and S6–S7 and Table S2). The positional effect of the *meso*-amine units on the intensity of the broad ICT bands is noteworthy; the ICT bands of the *meso-N*-amine derivatives **5M** are more intense than those of the *meso-C*-amine derivatives **11M**. These differences can be attributed to the slightly different characteristics of their LUMOs. As shown in Figure 4, the LUMO of **5Ni-m** possesses a degree of orbital coefficients on the *meso*-nitrogen atoms adjacent to the TPA units, whereas that of **11Ni-m** has virtually no orbital coefficient on the corresponding *meso*-carbon atoms. This indicates that the degree of overlap between the HOMO and LUMO of **5Ni-m** should be larger than that of **11Ni-m**. The TD-DFT results also support the subtle difference in the observed transition intensities; the calculated

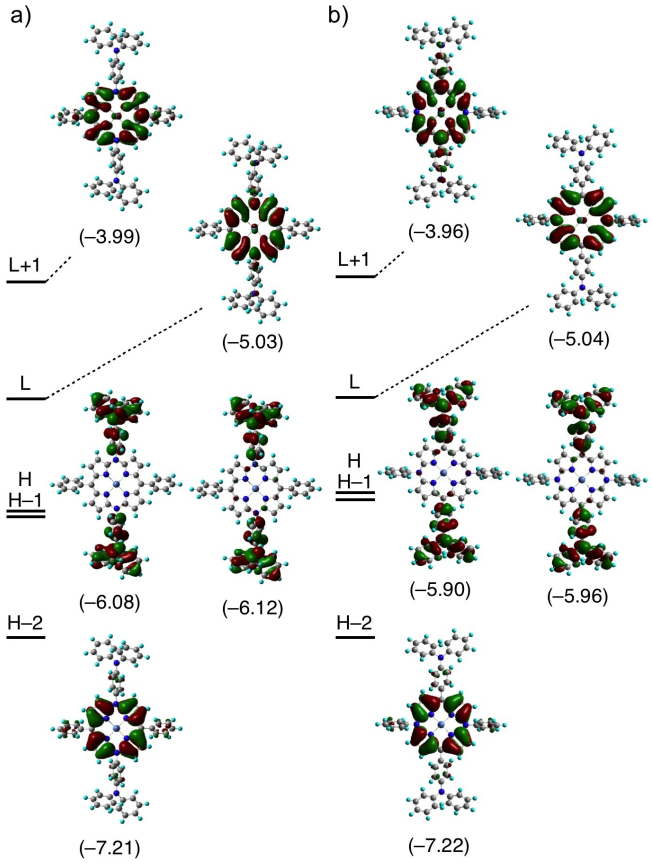

Figure 4. Selected Kohn-Sham orbitals and their energies (in eV) of a) **5Ni-m** and b) **11Ni-m** calculated by the DFT (B3LYP) method with the solvent effect (PCM, CH_2Cl_2). H = HOMO; L = LUMO.

oscillator strength for the HOMO-to-LUMO transition of **5Ni-m** ($f = 0.259$) was appreciably larger than that of **11Ni-m** ($f = 0.026$). The positional effect was not clearly observed for the symmetrically forbidden HOMO-to-LUMO transitions of the 20π TADAP derivatives, **3Ni-b** and **9Ni-b** (Figure 3a), because of the low intensity of these transitions; the calculated oscillator strengths for the HOMO-to-LUMO transition of **3Ni-m** and **9Ni-m** were 0.0001 and 0.0002, respectively (Table S2).

Electrochemical Properties. The redox potentials of M-TADAP-amine hybrids **4M** (M = Ni, Zn, Cu), **10M** (M = Ni, Cu), and **13Cu** in CH_2Cl_2 were measured using cyclic voltammetry (CV) with Bu_4NPF_6 as a supporting electrolyte. As shown in Figures 5 and S8, each voltammogram displays two reversible electrochemical processes corresponding to the 20π/19π and 19π/18π redox couples of the DAP ring with separated potentials ($\Delta E = E_{19\pi/18\pi} - E_{20\pi/19\pi}$) of 0.60-0.67 V. For the copper complexes, **4Cu**, **10Cu**, and **13Cu**, the 21π/20π redox couples were also observed in the range of $E_{1/2} = -1.92$ to -2.03 V vs. Fc/Fc^+. First, the effects of the central metal and peripheral amine units on the redox potentials are discussed. The following findings (i)–(iv) are notable. (i) For the hybrids having the same *meso*-substituents, the $E_{1/2}$ values were shifted in the positive direction in the order of M=Zn < Ni ~ Cu, corresponding to the electronegativity of the central metal.[19] (ii) For the hybrids having the same central metal, the $E_{1/2}$ values were shifted to the positive side in the order of *para*-NRR′ = $NTol_2$ (**b**) < NHPh (**c**) < NPh_2 (**a**), reflecting the differences in the electron-donating ability of these amine units.[20–23] (iii) For the hybrids having the same central metal and tertiary amine (TA) units, the $E_{1/2}$ values of the *meso*-*N*-TA derivatives (**4M-b**) were shifted slightly to the negative side compared with those of the *meso*-*C*-TA derivatives (**10M-b**). This small difference in the $E_{1/2}$ values cannot be attributed solely to the positional effect of the *meso*-aryl groups because the DFT calculations for the Ni-TADAP-TPA hybrids (Figures S6 and S7) indicated comparable HOMO and LUMO energies for the 20π (−4.37 eV for **3Ni-m**, −4.38 eV for **9Ni-m**) and 18π derivatives (−5.03 eV for **5Ni-m**, −5.04 eV for **11Ni-m**), respectively. It is therefore likely that a somewhat different electronic property of the remaining *meso*-aryl group, mesityl (**4M-b**) or phenyl (**10M-b**), was responsible for the observed difference. (iv) The number of *meso*-TA units had little influence on the redox potentials.

The cyclic voltammograms of all the M-TADAP-amine hybrids exhibited additional electrochemical processes at more positive potentials (> +0.3 V vs. Fc/Fc^+), which could be attributed to the amine-centered oxidation of the in-situ generated 18π-TADAP dications. The following features (i)–(iii) are worth noting. (i) The first anodic scan for the 18π *para*-NPh_2-substituted derivatives **5Ni-a**, **5Zn-a**, **5Cu-a**, **11Cu-a**, and **14Cu** showed irreversible peaks at $E_{pa} = +0.77$, +0.76, +0.77, +0.62, and +0.75 V (scan rate = 60 mV s^{-1}), respectively, whereas the first cathodic reverse-scan exhibited a new pair of peaks at more negative potentials. The E_{pa} values of **5M-a**, **11Cu-a**, and **14Cu** are more positive than that of triphenylamine ($E_{pa} = +0.60$ V under our measurement conditions; scan rate = 60 mV s^{-1}), reflecting the electron-withdrawing property of the 18π M-TADAP dication moiety. The electrochemical behavior of

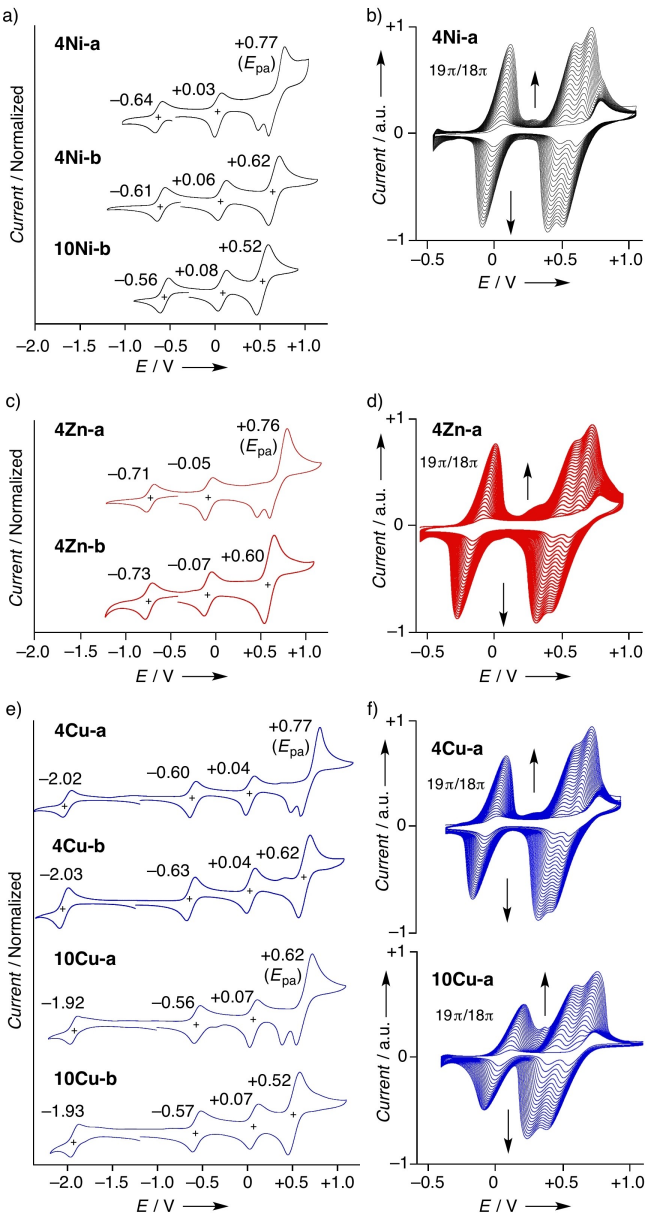

Figure 5. Cyclic voltammograms of M-TADAP-amine hybrids in CH_2Cl_2 with Bu_4NPF_6 as a supporting electrolyte. The potentials are referenced to a ferrocene/ferrocenium (Fc/Fc^+) couple. Half-wave potentials ($E_{1/2}$) are recorded for the reversible processes, and anodic peak potentials (E_{pa}) are recorded for the irreversible oxidation processes observed in the first anodic scan. The voltammograms of the first single scan (scan rate = 60 mV s^{-1}) are shown in a) **4Ni-a**,**b** and **10Ni-b**, c) **4Zn-a**,**b**, e) **4Cu-a**,**b** and **10Cu-a**,**b**. The voltammograms of the repeat scans (scan rate = 60 mV s^{-1}) are shown in b) **4Ni-a** (data from ref. 17), d) **4Zn-a**, f) **4Cu-a** and **10Cu-a**.

5M-a, **11Cu-a**, and **14Cu** will be discussed later. (ii) The voltammograms of the *para*-$NTol_2$-substituted derivatives **5M-b** (M = Ni, Zn, Cu) and **11M-b** (M = Ni, Cu) showed an additional reversible one-step, 2e redox couple in the range of $E_{1/2} = +0.52$ to +0.62 V, indicating that redox reactions on the two tertiary amine units proceeded reversibly and simultaneously. The generation of triarylammoniumyl radicals from **5M-b** (M = Ni, Zn) was supported by the spectroelectrochemical results (Figure S9); the electrochemical oxidation of **5M-b** in CH_2Cl_2

with Bu_4NPF_6 as the electrolyte at varying applied potentials in the range of +0.8 to +1.0 V (vs. Fc/Fc^+) resulted in a gradual increase in new absorption bands with λ_{max} values of 705–710 nm. Based on the spectroelectrochemical data reported for triarylamines,[24] the generated species were determined to be amine-centered radical cations of **5M-b**, as illustrated in Figure S9c. (iii) The *para*-NHPh-substituted derivatives **5Ni-c** and **5Cu-c** displayed an irreversible oxidation process at $E_{pa} = +0.63$ and +0.67 V, respectively, in the first anodic scan (Figure S8a); thus, the E_{pa} values were positively shifted compared with that of diphenylamine ($E_{pa} = +0.55$ V under our measurement conditions; scan rate = 60 mV s^{-1}). For **5M-c**, a new pair of peaks appeared during the reverse cathodic scans, as observed for **5M-a**.

We have previously reported the repeat CV scan results for **4Ni-a**, wherein two reversible redox processes appeared from the second cycle in the range of −0.5 to +1.0 V, in addition to the TADAP-centered 19π/18π redox couple (Figure 5b).[17] In the present study, we conducted repeat CV scans for the newly prepared M-TADAP-TPA hybrids, which exhibited similar electrochemical behavior (Figures 5d, f and S8d). For all of the TPA-containing hybrids, repetitive potential cycling resulted in a progressive increase in both the anodic and cathodic peak currents of the reversible redox processes. For **4M-a** and **10Cu-a**, the $E_{1/2}$ values after 20 scans (scan rate = 60 mV s^{-1}) were almost identical to those observed for the second scan. Two new redox processes appeared, with $E_{1/2}$ values of +0.47 and +0.54 V for **4Zn-a**, +0.47 and +0.57 V for **4Cu-a**, and +0.41 and +0.58 V for **10Cu-a**. This mode of electrochemical behavior can be rationalized by the immobilization of redox-active polymer deposits on the electrode surface. Indeed, poly**4M-a**-immobilized working electrodes, which had been repeatedly rinsed with CH_2Cl_2 and then placed in a cell filled with a CH_2Cl_2 solution containing only Bu_4NPF_6, presented characteristic voltammograms comprising the intrinsically same multiple redox couples (Figure S10a).

It is well known that the electrochemical oxidation of TPA generates a triphenylammoniumyl radical, which dimerizes at the *para* position to afford *N*,*N*,*N*′,*N*′-tetraphenylbenzidine after rapid elimination of two protons.[25] This type of coupling also occurs during the electrochemical oxidation of TPA-appended porphyrins.[4] It is therefore likely that the ammoniumyl radicals generated from the *para*-NPh_2-substituted derivatives **5M-a** (M = Ni, Zn, Cu), **11Cu-a**, and **14Cu** underwent intermolecular oxidative coupling at the *para* position of their *N*-phenyl rings to form benzidine-linked TADAP polymers after the furthest anodic oxidation (Scheme 6). This mechanism was strongly supported by the observation that the *para*-$NTol_2$-substituted derivatives **5M-b** and **11M-b** exhibited reversible one-step 2e redox processes and did not show any progressive increase in the electric currents during the repeat CV scans.

When compared with the reported $E_{1/2}$ values of the two reversible redox processes of *N*,*N*,*N*′,*N*′-tetraphenylbenzidine (+0.36 and +0.50 V vs. Fc/Fc^+; in MeCN, with Bu_4NPF_6)[26] and of an immobilized TPP-benzidine polymer (+0.29 and +0.49 V vs. Fc/Fc^+; in CH_2Cl_2, with Bu_4NPF_6),[4,27] those of the present TADAP-benzidine polymers (+0.49–0.53 and +0.60–0.65 V vs. Fc/Fc^+ in CH_2Cl_2, with Bu_4NPF_6) were appreciably shifted to the positive side. This is possibly due to the low HOMO level of the 18π DAP dication unit in the TADAP-benzidine polymers compared to that of the isoelectronic porphyrin unit in the TPP-benzidine polymer. The repeat CV scans of **13Cu** produced broadened voltammograms (Figure S8d), indicating that the rate of electron transfer on the electrode surface slowed down significantly as the degree of polymerization increased. We assume that the oxidative coupling at the four *meso*-TPA units of **13Cu** prompted electrochemical polymerization in multiple directions to form randomly linked benzidine networks.

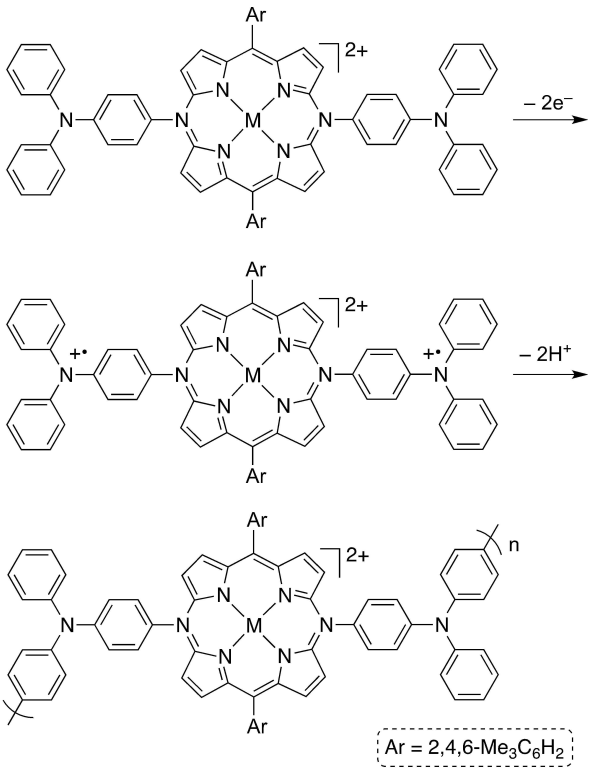

Scheme 6. Plausible mechanism of electrochemical polymerization of **5M-a**.

Repeat CV scans of the *para*-NHPh-substituted derivatives **4Ni-c** and **4Cu-c** also resulted in a progressively increasing electric current (Figure S8b). Two new redox processes appeared, with $E_{1/2}$ values of +0.44 and +0.57 V for poly**4Ni-c**, and +0.43 and +0.57 V for poly**4Cu-c** (Figure S10b), suggesting that the corresponding M-TADAP-benzidine polymers were formed on the electrode surface.[28] However, the electric currents observed for the new redox processes were saturated at shorter steps compared with those of the *para*-NPh_2-substituted counterpart poly**4M-a** (M = Ni, Cu), likely as a result of differing dimerization rate constants of amine radical cations generated from ArNHPh units in **5M-c** and $ArNPh_2$ units in **5M-a**.[29] This may also indicate the involvement of several reaction pathways due to the participation of the two N–H groups in **5M-c**.

CV measurements of poly**4M-a** (M = Zn, Cu), poly**4Cu-c**, and poly**10Cu-a** on the electrode were performed in the absence of monomers by varying scan rates in the range of 10 to

200 mV s^{-1} (Figure 6). Most of the M-TADAP-benzidine polymer films showed nearly symmetrical current responses, where both the anodic and cathodic peak currents increased with the increase in scan rate. These observations suggested that the TADAP-centered and benzidine-centered redox processes occurred in the deposited polymer films without any diffusion limits.

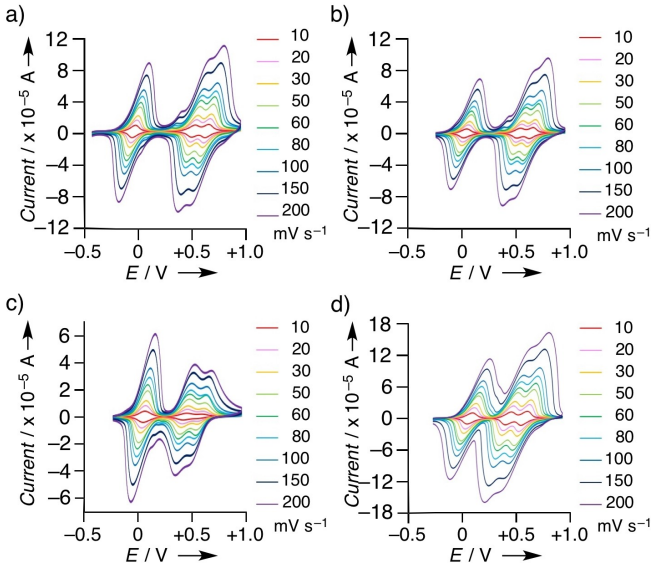

Figure 6. Scan-rate dependence of cyclic voltammograms in the range of −0.5 to +1.0 V vs. Fc/Fc$^+$ of the immobilized M-TADAP-benzidine polymers in CH_2Cl_2 with Bu_4NPF_6 as the electrolyte: a) poly**4Zn-a**, b) poly**4Cu-a**, c) poly**4Cu-c**, and d) poly**10Cu-a**.

To further investigate the electrochromic properties of the M-TADAP-benzidine polymer films, **4Cu-a** and **10Cu-a** were electrochemically polymerized on the surface of indium-tin-oxide (ITO) substrates. The resulting electrodes (poly**4Cu-a**/ITO and poly**10Cu-a**/ITO) were used for spectroelectrochemical measurements (Figures 7 and S12). When the applied potential was −0.6 V (vs. Ag/Ag$^+$), the poly**4Cu-a**/ITO displayed red color, derived from the 20π TADAP chromophore (λ_{max} = 450 and 529 nm). When the applied potential was increased from −0.6 to +1.6 V, the poly**4Cu-a**/ITO exhibited distinct color change from red to dark yellow (at +0.1 V) to bluish green (at +0.7 V) to dark blue (at +1.6 V). This electrochromic behavior was monitored by UV/vis/NIR absorption spectroscopy (Figure 7), which confirmed the stepwise changes to the 19π TADAP radical cation (λ_{max} = 388, 447, and 880 nm) to the 18π TADAP dication (λ_{max} = 393 and 631 nm) to the 18π TADAP-benzidine tetracation (λ_{max} = 393, 629, and 701 nm). It is worth noting that the reverse potential shift from +1.6 to −0.6 V turned the color from dark blue to red, with recovery of the absorption spectrum derived from the polymer consisting of the 20π TADAP chromophore. A similar electrochromic property was verified for

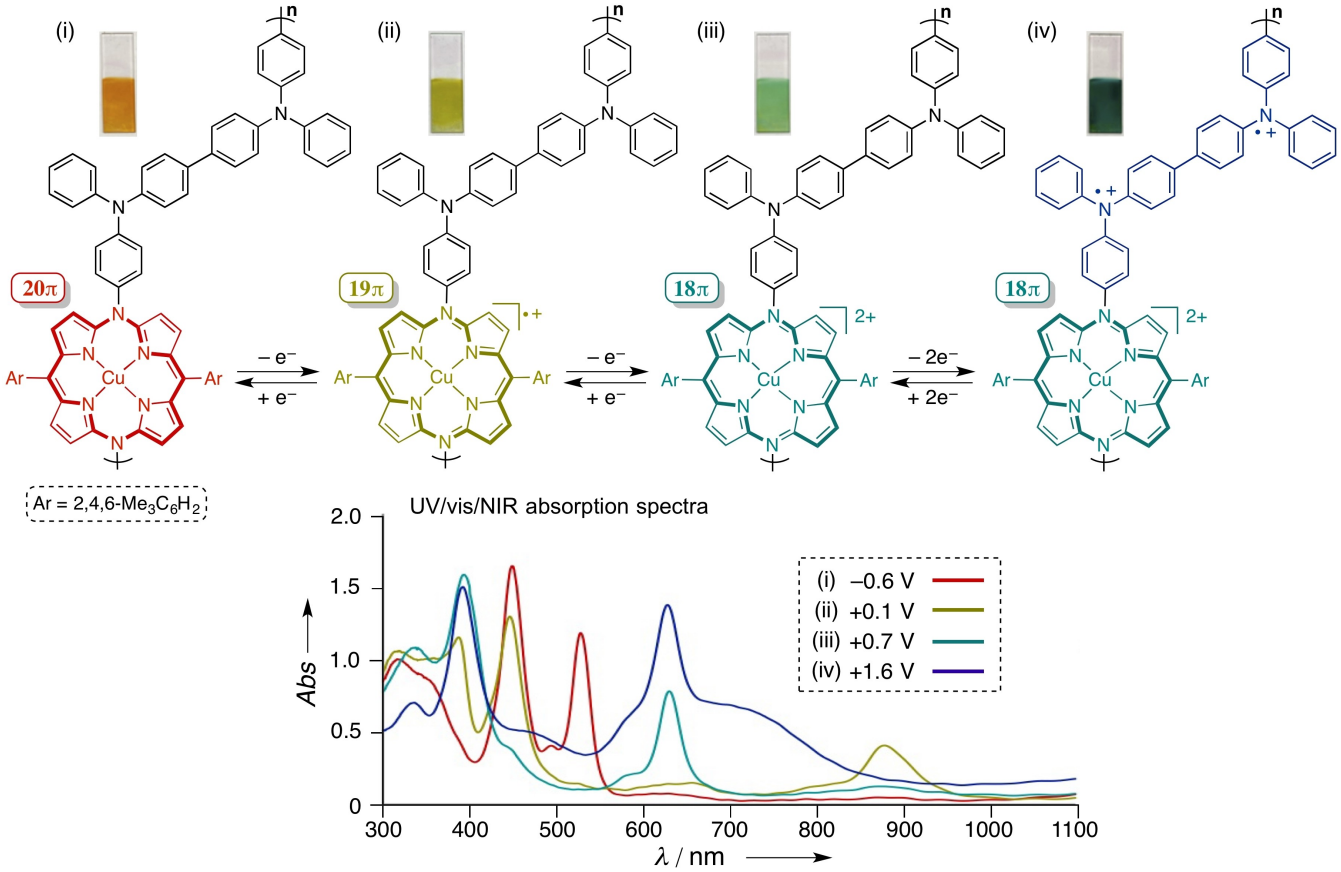

Figure 7. Color and spectral change in the poly**4Cu-a**/ITO electrode at applied potentials of (i) −0.6 V, (ii) +0.1 V, (iii) +0.7 V, (iv) +1.6 V vs. Ag/Ag$^+$.

the poly**10Cu-a**/ITO, which also demonstrated the concurrent color changes at the applied potentials (Figure S11).

Electrical Conductivity of M-TADAP-Benzidine Polymers

To measure the electrical conductivity of the M-TADAP-benzidine polymers, the sample films were immobilized between comb-shaped electrodes deposited on quartz glass substrates using CH_2Cl_2 solutions of **4M-a** (M = Ni, Zn, Cu), **4Ni-c**, **10Cu-a**, and **13Cu**, with Bu_4NPF_6 as the electrolyte. The progress of the electrochemical polymerization on the electrode was visually confirmed. UV/vis/NIR absorption spectroscopy results revealed that most of the DAP rings in the resulting M-TADAP-benzidine polymers were in the 18π-electron state. The current-voltage (*I*–*V*) characteristics of poly**4M-a**, poly**4Ni-c**, poly**10Cu-a**, and poly**13Cu** are shown in Figure S12. The electrical conductivity of a P3HT-deposited electrode [P3HT = poly(3-hexylthiophene)] was also measured as a reference, under the same conditions. As shown in Table S3, the electrical conductivities (σ) of the M-TADAP-benzidine polymers varied significantly depending on the central metal, amino linkages, and *meso*-substitution patterns, although the structure-conductivity relationship is not clearly understood at present. Among all the electrodes examined, poly**4Ni-a** exhibited the highest σ value of 2×10^{-3} S m^{-1}, which was larger by two or three orders of magnitude than the σ values observed for the other polymers. It is worth noting that the conductivity of poly**4Ni-a** is comparable with that of P3HT ($\sigma = 2\times10^{-3}$ S m^{-1}), a standard p-type polymer semiconductor. These results show that M-TADAP-benzidine polymers can serve as chemically tunable platforms for the development of DAP-based semiconducting polymer materials.

Conclusion

A series of covalently linked M-TADAP-amine hybrids (M = Ni, Zn, Cu) possessing a DAP ring in the 20π-, 19π-, or 18π-electron state were synthesized using the metal-templated cyclization approach to reveal the intrinsic effects of the central metal and peripheral amine units on the optical and redox properties of these hybrids. The obtained M-TADAP-amine hybrids exhibited characteristic π-π* electronic transitions reflecting the oxidation state of the DAP ring; the 18π TADAP dications displayed broad absorption bands in the NIR region, assigned to the ICT excitation from the amine-based HOMO to the DAP-based LUMO. The intensity of the ICT bands depended on the position of the peripheral tertiary amine (TA) moieties; *meso*-*N*-TA derivatives exhibited more intense ICT bands than *meso*-*C*-TA derivatives. The redox potentials of the M-TADAP-amine hybrids clearly reflected the electronic effects of the central metal and the peripheral amine moieties; the DAP-centered redox processes were positively shifted in the order of M = Zn < Ni ~ Cu and NRR′ = $NTol_2$ < NHPh < NPh_2. The structure of the amine units also exerted a significant impact on the electrochemical behavior of the M-TADAP-amine hybrids, and the *para*-NPh_2 derivatives were electrochemically polymerized after the DAP-centered 19π/18π redox process to afford the corresponding M-TADAP-benzidine polymers. The resulting polymers exhibited multiple reversible redox processes as DAP- and benzidine-centered redox reactions occurred over a range of 2.5 V. The Cu-TADAP-benzidine polymers deposited on the ITO electrode displayed the naked-eye detectable colorimetric responses to the applied potentials. The Ni-TADAP-benzidine polymer formed on a comb-shaped electrode exhibited the highest electrical conductivity, being 2×10^{-3} S m^{-1}, which was comparable with the conductivity of the P3HT-electrode measured under the same conditions. The present study highlights the considerable potential of M-TADAP-amine hybrids for providing a promising platform for the development of redox-switchable visible- and NIR-responsive sensitizers and conductive polymer materials.

Experimental Section

General Remarks: All melting points were recorded on a micro melting point apparatus and are uncorrected. The NMR spectra were recorded on 400 MHz (Agilent or Bruker) spectrometers. The ^{1}H and ^{13}C chemical shifts are reported in ppm as relative values vs. tetramethylsilane (in $CDCl_3$ and CD_2Cl_2) or a solvent residual signal (δ_H 7.16 ppm in C_6D_6), and the ^{31}P chemical shifts are reported in ppm vs. H_3PO_4. High-resolution mass (HRMS) spectra were measured on a Thermo Fisher Scientific EXACTIVE spectrometer (electron spray-quadrupole). The UV/Vis/NIR absorption spectra were measured on a JASCO V-530 spectrometer in the range of 300–1100 nm. The IR (Attenuated Total Reflection; ATR) spectra were obtained on a JASCO FT/IR4600 spectrometer. Redox potentials and electrochemical behavior were measured at room temperature on an ALS model 650E electrochemical workstation using a glassy carbon working electrode, a platinum wire counter electrode, and an Ag/Ag^+ [0.01 M $AgNO_3$, 0.1 M Bu_4NPF_6 (MeCN)] reference electrode. In the case of spectroelectrochemical measurements, a 1-mm quartz batch-cell equipped with the above-mentioned three electrodes was used. The ITO electrode purchased from Japan Cell Co. was washed with acetone and 2-propanol and then cleaned by a UV ozone cleaner. The UV/Vis/NIR absorption spectra of the polymer-coated ITO electrodes were measured using a bare ITO substrate as a reference. Thin-layer chromatography was performed with Kieselgel 60 F254, and preparative column chromatography was performed using Silica Gel 60 spherical, neutrality. All reactions were performed under an argon or nitrogen atmosphere unless otherwise noted. For all the synthesis and characterization data of new compounds are reported in the Supporting Information.

X-ray Crystallographic Analysis: Single crystals of **4Cu-c** were grown from CH_2Cl_2-hexane. Selected crystallographic data are as follows. Trigonal, *R*-3, $a = 22.8506(3)$ Å, $b = 22.8506(3)$ Å, $c = 30.4283(4)$ Å, $V = 13759.5(4)$ Å^3, $Z = 9$, $\rho_{calcd} = 1.225$ g cm^{-3}, $\mu = 1.28$ cm^{-1}, collected 83951, independent 7025, parameters 361, $R_w = 0.2091$ (all data), $R_1 = 0.0642$ ($I > 2.0\sigma(I)$), GOF = 1.059. https://www.ccdc.cam.ac.uk/services/structures?id=doi:10.1002/cplu.202100429 Deposition Number 2108277 contain(s) the supplementary crystallographic data for this paper. These data are provided free of charge by the joint Cambridge Crystallographic Data Centre and Fachinformationszentrum Karlsruhe Access Structures service www.ccdc.cam.ac.uk/structures.

DFT Calculations: The geometries were optimized with the density functional theory (DFT) method. The basis sets used for the

optimization were 6-311G(d,p) basis set[30] for H, C, and N and the Wachters-Hay all electron basis set[31] supplemented with one f-function (exponent: 1.29 for Ni, 1.62 for Zn). The functional of DFT was the Becke, three-parameter, Lee-Yang-Parr (B3LYP) exchange-correlation functional.[32] The optimized geometries were confirmed to be minima by vibrational analysis. The Cartesian coordinates and computed total energies are summarized in Table S1. The excitation energies and oscillator strengths listed in Table S2 were computed with the time-dependent density functional theory (TD-DFT) method, where a Minnesota global hybrid functional M06-2X[33] was used. The solvent effects were incorporated in both the DFT and TD-DFT calculations using the polarizable continuum model (PCM) with the integral equation formalism variant.[34] All the calculations were carried out using the Gaussian 16 suite of programs.[35]

EPR Measurements: The electron paramagnetic resonance (EPR) spectra were measured at room temperature by using a JEOL JES-FA200 spectrometer equipped with an OXFORD ESR900 He-flow cryostat. All samples were prepared as a 0.1 mM solution in CH_2Cl_2. After three freeze-pump-thaw cycles, the solution sample in a quartz tube was sealed by frame. Spectral simulation was performed using EasySpin,[36] which is a MATLAB toolbox meant for this. The static magnetic field and microwave frequency were measured by an Echo Electronics EFM-2000 gauss meter and a TakedaRiken TR5212 microwave counter, respectively.

Electrical Conductivity Measurements: Current-voltage (*I–V*) characteristics of the sample films formed between comb-shape electrodes deposited on quartz glass substrates were measured by a source meter (KEITHLEY, 2602B). The height and interelectrode distance of the electrodes on substrate were 100 nm and 50 μm, respectively. Conductance (*G*) of the film between the electrodes was obtained from the slope of *I–V* curve. Conductivity (σ) of the film was estimated using the *G* and the film volume expanded between the electrodes.

Acknowledgements

This work was supported by JSPS KAKENHI (18H01961 to YM, and 18K05036, 21K04980 to HN) and the Research Program of "Five-star Alliance" in "NJRC Mater. & Dev." (20214029), a research grant of Nihon Kagaku Kenkyukai (492(R)) to TI. We also express our gratitude to the SPring-8 synchrotron, where synchrotron radiation experiments were performed at the BL40XU beamline with the approval of the Japan Synchrotron Radiation Research Institute (JASRI) (proposals 2020A0557, 2020A0834, 2020A1056, 2020A1644, 2020A1656, and 2021A1592).

Conflict of Interest

The authors declare no conflict of interest.

Keywords: dyes/pigments · EPR spectroscopy · polymer films · porphyrinoids · redox chemistry

[1] For example, see: a) G. Y. Gao, Y. Chen, X. P. Zhang, *J. Org. Chem.* **2003**, *68*, 6215–6221; b) M. E. El-Khouly, J. B. Ryu, K.-Y. Kay, O. Ito, S. Fukuzumi, *J. Phys. Chem. C* **2009**, *113*, 15444–15453; c) C.-Y. Huang, C.-Y. Hsu, L.-Y. Yang, C.-J. Lee, T.-F. Yang, C.-C. Hsu, C.-H. Ke, Y. O. Su, *Eur. J. Inorg. Chem.* **2012**, *2012*, 1038–1047; d) Y. Zhang, S. Zhang, L. Yao, L. Qin, L. Nian, Z. Xie, B. Yang, L. Liu, Y. Ma, *Eur. J. Inorg. Chem.* **2014**, *2014*, 4852–4857; e) Y. Tang, Y. Wang, X. Li, H. Ågren, W.-H. Zhu, Y. Xie, *ACS Appl. Mater. Interfaces* **2015**, *7*, 27976–27985; f) A. Covezzi, A. O. Biroli, F. Tessore, A. Forni, D. Marinotto, P. Biagini, G. D. Carlo, M. Pizzotti *Chem. Commun.* **2016**, *52*, 12642–12645; g) M. Cariello, S. M. Abdalhadi, P. Yadav, J.-D. Decoppet, S. M. Zakeeruddin, M. Grätzel, A. Hagfeldt, G. Cooke, *Dalton Trans.* **2018**, *47*, 6549–6556; h) R. Pudi, C. Rodríguez-Seco, A. Vidal-Ferran, P. Ballester, E. Palomares, *Eur. J. Org. Chem.* **2018**, *2018*, 2064–2070; i) T. Higashino, Y. Kurumisawa, H. Iiyama, H. Imahori, *Chem. Eur. J.* **2019**, *25*, 538–547; j) M. Sankar, P. Rathi, A. Ganesan, S. Seetharaman, P. A. Karr, F. D'Souza, *J. Phys. Chem. B* **2020**, *124*, 5723–5729; k) S. Kotteswaran, P. Ramasamy, *New J. Chem.* **2021**, *45*, 2453–2462, and references therein.
[2] C.-W. Huang, K. Y. Chiu, S.-H. Cheng, *Dalton Trans.* **2005**, *34*, 2417–2422.
[3] M. D. Funes, D. A. Caminos, M. G. Alvarez, F. Fungo, L. A. Otero, E. N. Durantini, *Environ. Sci. Technol.* **2009**, *43*, 902–908.
[4] N. K. Subbaiyan, I. Obraztsov, C. A. Wijesinghe, K. Tran, W. Kutner, F. D'Souza, *J. Phys. Chem. C* **2009**, *113*, 8982–8989.
[5] M. Gervaldo, M. Funes, J. Durantini, L. Fernandez, F. Fungo, L. Otero, *Electrochim. Acta* **2010**, *55*, 1948–1957.
[6] J. Durantini, G. M. Morales, M. Santo, M. Funes, E. N. Durantini, F. Fungo, T. Dittrich, L. Otero, M. Gervaldo, *Org. Electron.* **2012**, *13*, 604–614.
[7] K. Noworyta, W. Kutner, C. A. Wijesinghe, S. G. Srour, F. D'Souza, *Anal. Chem.* **2012**, *84*, 2154–2163.
[8] M. Urbani, M. Grätzel, M. K. Nazeeruddin, T. Torres, *Chem. Rev.* **2014**, *114*, 12330–12396.
[9] R. B. Ambre, S. B. Mane, G.-F. Chang, C.-H. Hung, *ACS Appl. Mater. Interfaces* **2015**, *7*, 1879–1891.
[10] J. Durantini, M. B. Suarez, M. Santo, E. Durantini, T. Dittrich, L. Otero, M. Gervaldo, *J. Phys. Chem. C* **2015**, *119*, 4044–4051.
[11] X.-M. Hu, Z. Salmi, M. Lillethorup, E. B. Pedersen, M. Robert, S. U. Pedersen, T. Skrydstrup, K. Daasbjerg, *Chem. Commun.* **2016**, *52*, 5864–5867.
[12] B. Fu, X. Dong, X. Yu, Z. Zhang, L. Sun, W. Zhu, X. Liang, H. Xu, *New J. Chem.* **2021**, *45*, 2141–2146.
[13] a) J. Mack, N. Kobayashi, *Chem. Rev.* **2011**, *111*, 281–321; b) Y. Matano, *Chem. Rev.* **2017**, *117*, 3138–3191.
[14] a) T. Satoh, M. Minoura, H. Nakano, K. Furukawa, Y. Matano, *Angew. Chem. Int. Ed.* **2016**, *55*, 2235–2238; *Angew. Chem.* **2016**, *128*, 2275–2278; b) K. Sudoh, T. Satoh, T. Amaya, K. Furukawa, M. Minoura, H. Nakano, Y. Matano, *Chem. Eur. J.* **2017**, *23*, 16364–16373; c) H. Ochiai, K. Furukawa, H. Nakano, Y. Matano, *J. Org. Chem.* **2021**, *86*, 2283–2296.
[15] K. Sudoh, T. Hatakeyama, K. Furukawa, H. Nakano, Y. Matano, *J. Porphyrins Phthalocyanines* **2018**, *22*, 542–551.
[16] M. Mutoh, K. Sudoh, K. Furukawa, M. Minoura, H. Nakano, Y. Matano, *Asian J. Org. Chem.* **2019**, *8*, 352–355.
[17] K. Sudoh, Y. Satoh, K. Furukawa, H. Nakano, Y. Matano, *J. Porphyrins Phthalocyanines* **2020**, *24*, 286–297. The preliminary results for **3Ni-a**, **4Ni-a**, and **5Ni-a** and Ni-TADAP-amine hybrids substituted with p-NMe_2 group (**P2**; R = NMe_2, M = Ni, Cu) were reported in this paper.
[18] The ^{1}H NMR spectrum of **11Ni-b** could not be measured clearly because of contamination of a small amount of the 19π radical **10Ni-b** generated in solution. However, the 18π-electron state of **11Ni-b** was confirmed by its UV/vis absorption spectrum shown in Figure 3a.
[19] Electronegativity (Pauling scale): 1.65 for Zn; 1.91 for Ni; 1.90 for Cu.
[20] Oxidation potentials (anodic peak potentials; E_{pa}) of Ph_3N and Tol_3N in MeCN were reported to be +0.92 V and +0.75 V vs. SCE, respectively (scan rate = 0.13 V s^{-1}); E. T. Seo, R. F. Nelson, J. M. Fritsch, L. S. Marcoux, D. W. Leedy, R. N. Adams, *J. Am. Chem. Soc.* **1966**, *88*, 3498–3503. These values are converted to +0.54 V and +0.37 V vs. Fc/Fc+, respectively, using a reference potential of +0.38 V (Fc/Fc$^+$ vs. SCE in MeCN with Bu_4NClO_4; ref. 23).
[21] The E_{pa} value of Ph_2NH in MeCN with Bu_4NPF_6 was reported to be +0.83 V vs. aq. SCE or +0.52 V vs. Fc/Fc$^+$ (scan rate = 0.2 V s^{-1}); H. Yang, A. J. Bard, *J. Electroanal. Chem.* **1991**, *306*, 87–109.
[22] Nicewicz et al. reported the E_{pa} value of Ph_2NH in MeCN as +0.92 V vs. SCE; H. G. Roth, N. A. Romero, D. A. Nicewicz, *Synlett* **2016**, *27*, 714–723. This value is converted to +0.52 V vs. Fc/Fc$^+$ using a reference potential of +0.40 V (Fc/Fc$^+$ vs. SCE in MeCN with Bu_4NPF_6; ref. 23).
[23] N. G. Connelly, W. E. Geiger, *Chem. Rev.* **1996**, *96*, 877–910.
[24] Electrochemical oxidation of triarylamines (R_3N) has been studied by electrospectroscopy. The λ_{max} values reported for the radical cations derived from R_3N (R = Ph, Tol) are in the range of 340 to 675 nm. For example, see: a) S. Amthor, B. Noller, C. Lambert, *Chem. Phys.* **2005**, *316*,

141–152; b) K. Y. Chiu, T. X. Su, J. H. Li, T.-H. Lin, G.-S. Liou, S.-H. Cheng, *J. Electroanal. Chem.* **2005**, *575*, 95–101; c) O. Yurchenko, D. Freytag, L. zur Borg, R. Zentel, J. Heinze, S. Ludwigs, *J. Phys. Chem. B* **2012**, *116*, 30–39.

[25] For example, see: a) R. N. Adams, *Acc. Chem. Res.* **1969**, *2*, 175–180; b) S. C. Creason, J. Wheeler, R. F. Nelson, *J. Org. Chem.* **1972**, *37*, 4440–4446; c) R. F. Nelson, R. H. Philp, *J. Phys. Chem.* **1979**, *83*, 713–716; d) K. Sreenath, C. V. Suneesh, V. K. R. Kumar, K. R. Gopidas, *J. Org. Chem.* **2008**, *73*, 3245–3251; e) O. Yurchenko, D. Freytag, L. zur Borg, R. Zentel, J. Heinze, S. Ludwigs, *J. Phys. Chem. B* **2012**, *116*, 30–39. See also ref. 18.

[26] N. A. Macías-Ruvalcaba, D. H. Evans, *J. Phys. Chem. C* **2007**, *111*, 5805–5811.

[27] In ref. 4, the $E_{1/2}$ values of the immobilized TPP-benzidine polymer were reported to be +0.75 V and +0.95 V vs. SCE in 1,2-dichloroethane with Bu_4NPF_6. These values are converted using a Fc/Fc^+ reference potential of +0.46 V vs. SCE (in CH_2Cl_2 with Bu_4NPF_6; ref. 23).

[28] a) W. Kemula, B. Behr, J. Taraszewska, *J. Electroanal. Chem.* **1975**, *65*, 651–659; b) M. Thanneermalai, T. Jeyaraman, C. Sivakumar, A. Gopalan, T. Vasudevan, T. C. Wen, *Spectrochim. Acta Part A* **2003**, *59*, 1937–1950.

[29] The dimerization rate constants of cation radicals arising from Ph_2NH and Ph_3N were reported to be $0.2–1.0\times10^6\ M^{-1}s^{-1}$ and $1.8–3\times10^3\ M^{-1}s^{-1}$, respectively. See: a) H. G. Yang, A. J. Bard, *J. Electroanal. Chem.* **1991**, *306*, 87–109; b) D. Larumbe, I. Gallardo, C. P. Andrieux, *J. Electroanal. Chem.* **1991**, *304*, 241–247; c) M. Oyama, K. Nozaki, S. Okazaki, *Anal. Chem.* **1991**, *63*, 1387–1392; d) M. Oyama, T. Higuchi, S. Okazaki, *J. Chem. Soc. Perkin Trans. 2* **2001**, 1287–1293.

[30] R. Krishnan, J. S. Binkley, R. Seeger, J. A. Pople, *J. Chem. Phys.* **1980**, *72*, 650–654.

[31] a) A. J. H. Wachters, *J. Chem. Phys.* **1970**, *52*, 1033–1036; b) P. J. Hay, *J. Chem. Phys.* **1977**, *66*, 4377–4384; c) K. Raghavachari, G. W. Trucks, *J. Chem. Phys.* **1989**, *91*, 1062–1065.

[32] a) A. D. Becke, *J. Chem. Phys.* **1993**, *98*, 5648–5652; b) C. Lee, W. Yang, R. G. Parr, *Phys. Rev. B* **1988**, *37*, 785–789.

[33] Y. Zhao, D. G. Truhlar, *Theor. Chem. Acc.* **2008**, *120*, 215–241.

[34] E. Cancès, B. Mennucci, J. Tomasi, *J. Chem. Phys.* **1997**, *107*, 3032–3041.

[35] M. J. Frisch, G. W. Trucks, H. B. Schlegel, G. E. Scuseria, M. A. Robb, J. R. Cheeseman, G. Scalmani, V. Barone, G. A. Petersson, H. Nakatsuji, X. Li, M. Caricato, A. V. Marenich, J. Bloino, B. G. Janesko, R. Gomperts, B. Mennucci, H. P. Hratchian, J. V. Ortiz, A. F. Izmaylov, J. L. Sonnenberg, D. Williams-Young, F. Ding, F. Lipparini, F. Egidi, J. Goings, B. Peng, A. Petrone, T. Henderson, D. Ranasinghe, V. G. Zakrzewski, J. Gao, N. Rega, G. Zheng, W. Liang, M. Hada, M. Ehara, K. Toyota, R. Fukuda, J. Hasegawa, M. Ishida, T. Nakajima, Y. Honda, O. Kitao, H. Nakai, T. Vreven, K. Throssell, J. A. Montgomery, Jr., J. E. Peralta, F. Ogliaro, M. J. Bearpark, J. J. Heyd, E. N. Brothers, K. N. Kudin, V. N. Staroverov, T. A. Keith, R. Kobayashi, J. Normand, K. Raghavachari, A. P. Rendell, J. C. Burant, S. S. Iyengar, J. Tomasi, M. Cossi, J. M. Millam, M. Klene, C. Adamo, R. Cammi, J. W. Ochterski, R. L. Martin, K. Morokuma, O. Farkas, J. B. Foresman, D. J. Fox, *Gaussian 16, Revision C.01*; Gaussian, Inc., Wallingford CT, 2019.

[36] S. Stoll, A. Schweiger, *J. Magn. Reson.* **2006**, *178*, 42–55.

Manuscript received: September 26, 2021
Revised manuscript received: October 9, 2021
Accepted manuscript online: October 11, 2021